A computational tool integrating host immunity with antibiotic dynamics to study tuberculosis treatment

Elsje Pienaar, Nicholas A. Cilfone, Philana Ling Lin, Veronique Dartois, Joshua T. Mattila, Russ Butler, JoAnne L. Flynn, Denise E. Kirschner and Jennifer J. Linderman

1. Model calibration, validation and implementation

1.1. Determination of vascular source micro-compartment (VSM) density

Physiological vascular density has been measured at 170-285 capillaries/mm^2 in 2D slices of tissue [1,2] or 293 cm^2/cm^3 (3D surface area of blood vessels per volume of tissue)[3]. We also measured the vascular density in a sample of normal non-human primate lung tissue, although tissue compression artifacts when taking slices of normal lung tissue are likely to lead to underestimation of vascular density in this sample. VSM density in *GranSim* is defined as a percentage of the total grid compartments. We can calculate the number of vascular sources per mm^2 from this definition to compare to 2D literature values. To compare to the 3D literature value, we approximate the 3D density represented by our 2D grid (Figure S1-A) using stereology, a technique used to estimate 3D tissue composition from 2D slices[4]. The method places arcs on a grid overlaid onto an image, and extrapolates the vascular surface per volume of tissue from the number of intersections between arcs and vascular walls. We also apply stereology to the sample of normal NHP lung (Figure S1-B) to get a 3D density estimate for NHP lung tissue. To interpret the image of normal NHP lung and identify which areas are blood vessels, air sacs and lung tissue, we use image classification from geographic information system (GIS, Figure S1-C). Below we elaborate on each method.

Stereology. We use the Grid Cycloid Arc plug-in for *ImageJ* for stereological analysis with a 20x20 grid for arc placement[5,6]. We acknowledge that stereology was not developed for use on *in silico* images, and that our 2D grid assumes all vascular sources are perfectly cross-sectioned (no longitudinal sections).

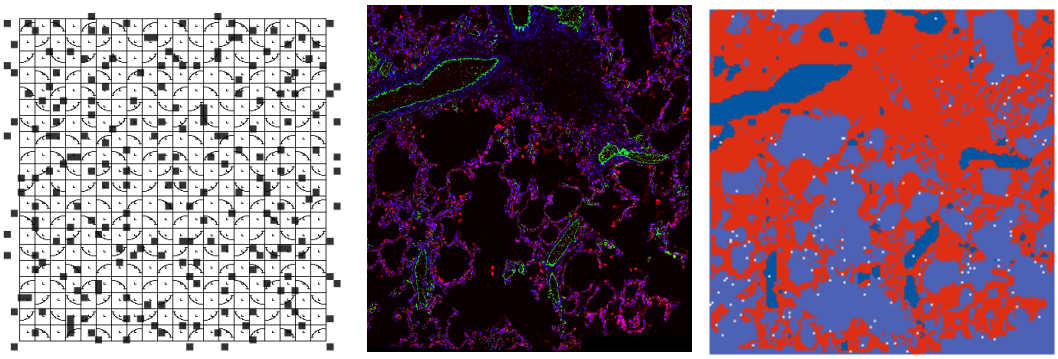

A B C

Figure S1: *Vascular source density estimation. (A) Representative image of VSM locations in GranSim with arcs used for stereology shown on the overlaid grid. Black squares indicate VSMs and the stereology grid is placed within a "counting frame" smaller than the original image, as per the method description[4] (B) Fluorescence microscopy image of normal lung tissue. Green is von Willebrand factor (vascular marker); red is B-actin; blue is cell nuclei stained with DRAQ5 (a DNA stain). (C) ArchGIS 10.1 classification of the microscopy image at the same scale as original image. Dark blue is blood vessels; light blue is air sacs; red is lung tissue; white dots are pixels of mixed classes (i.e. "edge" pixels) and comprise <1% of total.*

Image classification of the microscopy digital image. For the NHP lung vascular density estimate, we use a fluorescence microscopy image of normal lung tissue stained for von Willebrand factor, B-actin and cell nuclei. The image was imported into a geographic information system (GIS) program, ArcGIS 10.1. We created training sites for blood, tissue, and air as identified by microscopy (ArcGIS 10.1, on the imported microscopy image). This produced a digital, classified image measuring 200 x 200 (40,000) pixels referenced to the same spatial scale as the original image. By creating an internally consistent reference system relevant to the original image, scale (distances and pixel size) remains consistent. Thus, the classified image reveals accurate spatial and areal relationships of the different tissues classes. The resultant ASCII file (from the classified image) is imported into Matlab for further analysis. The classified image (Figure S1-C) is used for stereological analysis.

Results. Numerical data on vascular density in normal human or non-human primate lungs are limited. We therefore base our vascular density parameter on three pieces of information: (1) vascular density values in the literature, (2) our estimate of 3D vascular density in an NHP lung sample, (3) ability of the integrated model to reproduce rabbit antibiotic penetration data[7]. Using this information to constrain the vascular density parameter, we selected a density of 8.8%. This value has a 2D density of 220 capillaries/mm^2, which is within range of literature estimates (170-285 capillaries/mm^2). The 3D vascular density represented by this density parameter, as determined by stereology, is 185 ± 13 cm^2/cm^3 (mean ± SD; N = 3)

which is lower than the literature value of 293 cm^2/cm^3, and as expected, higher than our estimate from the NHP lung sample (50 cm^2/cm^3).

1.2. GranSim calibration for 200x200 grid size

GranSim has been calibrated to match per granuloma CFU curves measured in NHPs on a 100x100 simulation grid[8,9] (Cilfone et al., submitted 2014). In order to achieve more realistic granuloma sizes for use in this work, we recalibrated the model to the same NHP data for a 200x200 grid size. The calibrated control parameter set is given in Appendix A and model results are plotted with NHP data in Figure S2.

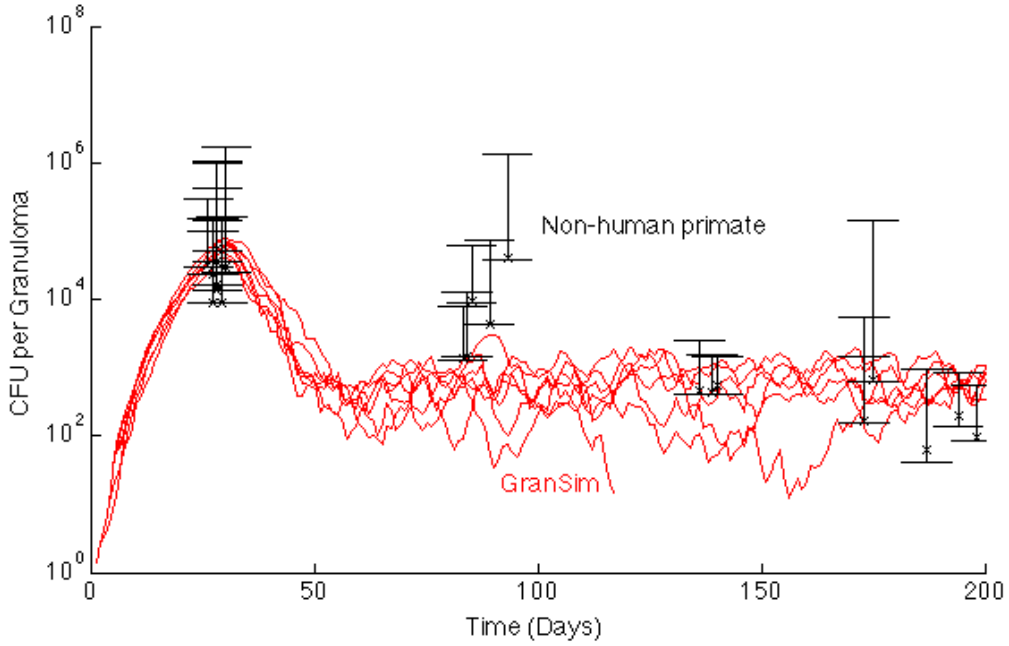

Figure S2: *Time course of CFU per granuloma for NHP (black) as well as GranSim (red) using the parameters in Appendix A. The model captures the high early peak (~30 d.p.i) before the onset of adaptive immunity, and the long term stabilization of CFU numbers after ~100 d.p.i.*

1.3. GranSim validation

As in previous published versions of *GranSim*[10-12], the larger grid format version used here is able to reproduce a range of granuloma-scale infection outcomes and granuloma phenotypes, including outcomes observed in TNF, IL-10 and IFNγ knock-out mice [13-15] (Figure S3).

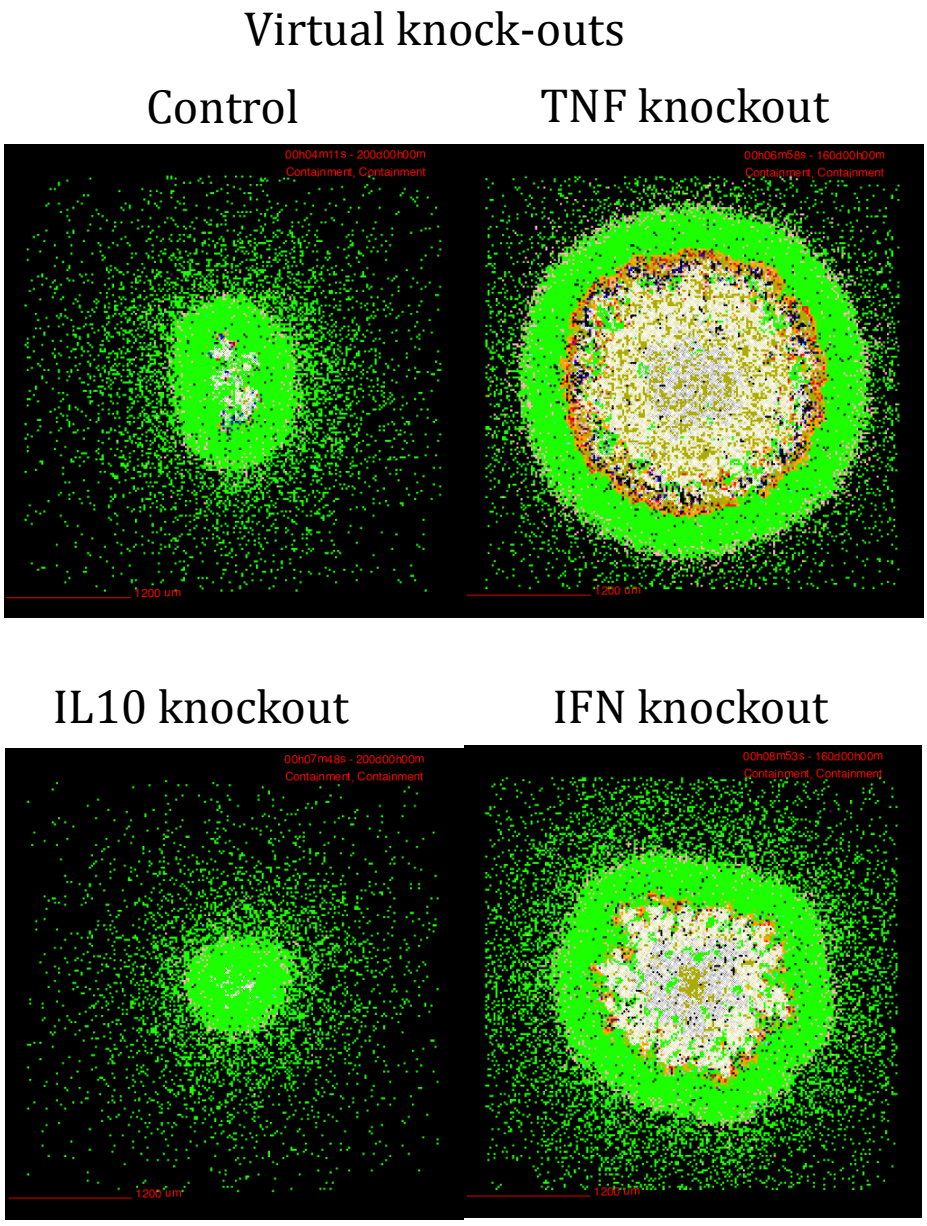

Figure S3: *Virtual TNF, IL-10 and IFNγ knockouts.. Compared to control granulomas (small with some caseation and localized bacterial growth), TNF and IFNγ knockouts show excessive bacterial growth and caseation, and large granulomas. IL-10 knockout granulomas resemble WT granulomas but with reduced bacterial growth and increased inflammation.*

1.4. Tunable resolution

Previous versions of *GranSim* focused on understanding the roles of TNF and IL-10 cytokine dynamics at a molecular scale and how receptor-ligand trafficking events (modeled as a system of non-linear ordinary differential equations (ODEs)) influenced infection outcomes[10,11]. Although many TNF and IL-10 events were identified as critical to control of infection, our focus in this work is to understand issues that arise during antibiotic treatment at the single granuloma level, and antibiotic dynamics add another level of model complexity. Thus, we apply the concept of tunable resolution to our model to not only retain our understanding of the roles of TNF and IL-10 during infection but also reduce model complexity and computational burden[16]. Our methods are motivated by the sensitivity analysis results that we performed in [10] to identify key model features. Briefly, the system of ODEs in [10] is replaced with the following equations describing the change in soluble TNF and soluble IL-10 concentrations in a compartment containing an agent:

$$\frac{d[sTNF]}{dt} = k'_{sTNF} - k_{cTNF}\left(\frac{[sTNF]}{K_{DT1} * \frac{N_{AV}}{V} + [sTNF]} - \frac{[sTNF]}{K_{DT2} * \frac{N_{AV}}{V} + [sTNF]}\right)$$

$$\frac{d[sIL10]}{dt} = k'_{sIL10} - k_{cIL10}\left(\frac{[sIL10]}{K_{DI} * \frac{N_{AV}}{V} + [sIL10]}\right)$$

Where k'_{sTNF} and k'_{sIL10} are the apparent secretion rates of TNF and IL-10, k_{cTNF} and k_{cIL10} are the apparent rate constants for consumption (which incorporate estimates for total receptors and any scaling factors for both TNF and IL-10), and K_{DT1}, K_{DT2}, and K_{DI} are affinities for TNFR1, TNFR2, and IL-10R respectively. Each quotient represents the bound fraction of surface receptors assuming a pseudo-steady state.

Additionally, we re-write probability functions that relied on molecular scale details in terms of soluble TNF and IL-10 concentrations:

$$P_{NF\kappa B} = \begin{cases} 0 & \frac{[sTNF]}{K_{DT1} * \frac{N_{AV}}{V} + [sTNF]} < \tau'_{NF\kappa B} \\ 1 - e^{-k'_{NF\kappa B}\left(\frac{[sTNF]}{K_{DT1} * \frac{N_{AV}}{V} + [sTNF]} - \tau'_{NF\kappa B}\right)\Delta t} & \frac{[sTNF]}{K_{DT1} * \frac{N_{AV}}{V} + [sTNF]} \geq \tau'_{NF\kappa B} \end{cases}$$

$$P_{apop} = \begin{cases} 0 & \left(\frac{[sTNF]}{K_{DT1} * \frac{N_{AV}}{V} + [sTNF]}\right) f_{int} < \tau'_{apop} \\ 1 - e^{-k'_{apop}\left(\left(\frac{[sTNF]}{K_{DT1} * \frac{N_{AV}}{V} + [sTNF]}\right) f_{int} - \tau'_{NF\kappa B}\right)\Delta t} & \left(\frac{[sTNF]}{K_{DT1} * \frac{N_{AV}}{V} + [sTNF]}\right) f_{int} \geq \tau'_{apop} \end{cases}$$

$k'_{NF\kappa B}$, k'_{apop}, $\tau'_{NF\kappa B}$ and τ'_{apop} are modified rate constants and thresholds for TNF-induced NF-κB activation and apoptosis, respectively, while f_{int} is a partition factor for estimating internalized bound receptors from the pseudo-steady state estimate of surface bound receptors. These resulting rate constants and parameters can be estimated from their corresponding parameters when the molecular scale detail is returned to the model (our computational model allows these sub-models to be turned on or off).

Lastly, inhibition of TNF synthesis by IL-10 is reduced to a simple dose dependence function based on the soluble IL-10 concentration in the compartment.

$$k'_{sTNF} = \frac{1}{1 + e^{\frac{\log[sIL10] + \alpha}{\beta}}}$$

Where k'_{sTNF} is the apparent secretion rate of TNF, α is the threshold parameter, and β is the shape parameter. These parameters are calculated directly from results of the system of ODEs. These new model parameter values are given in Table S1.

Table S1: Tunable resolution parameters.

Parameter	**Value**	**Unit**
Apparent TNF consumption rate	0.00077	s^{-1}
Apparent IL-10 consumption rate	0.0004	s^{-1}
Partition factor for estimating internalized bound receptors	11.3	-
Threshold for IL-10 inhibition of TNF secretion	-1.93	-
Shape parameter for IL-10 inhibition of TNF secretion	0.181	-
Apparent TNF secretion rate by macrophages	1.5	Molecules/s
Apparent IL-10 secretion rate by activated macrophages	0.3	Molecules/s
Apparent IL-10 secretion rate by infected macrophages	0.02	Molecules/s
Apparent TNF secretion rate by IFNg producing T-cells	0.15	Molecules/s
Apparent TNF secretion rate by cytotoxic T-cells	0.015	Molecules/s
Apparent IL-10 secretion rate by regulatory T-cells	0.739	Molecules/s
Affinity of TNF for TFNR1	1.9×10^{-11}	M
Affinity of IL-10 for IL-10R	4.56×10^{-10}	M

1.5. Spectral methods for solving diffusion equations

Spectral methods for solving PDEs are a class of collocation methods that analyze the discretized system in a global instead of a local manner[17-21]. The solution to the entire system is assumed by a basis function and time-varying coefficients are determined such that the solution to the system is satisfied. Importantly, spectral methods reduce PDEs to ODEs, reducing the computational burden of the numerical approximation[20]. We adapt the basic method for our needs to allow insulating boundary conditions and apply simple smoothing pre-processing steps to limit errors associated with discontinuous concentration fields [22] (Cilfone et al., submitted 2014).

2. Uncertainty/Sensitivity Analyses and Classification

2.1.Sensitivity analyses: PRCC and eFAST results

Parameter ranges for the host-specific PRCC are given in Appendix A in the main text. Parameter ranges for the antibiotic-specific PRCC are given in Appendix E in the main text. PRCC identifies model parameters that significantly correlate with model outcomes. Significant host (Table S2) and antibiotic (Table S3) parameters are shown. Host parameters are grouped into categories corresponding to those discussed in Table 1 in the main text and the categories for significant parameters are indicated in Table S2.

The one additional parameter identified as significant by eFAST that was not identified by PRCC is the intercompartmental clearance rate constant (Q). This parameter was shown to significantly contribute to variation in the time to clearance ($p<0.05$). There is no evidence of a non-monotonic relationship between Q and time to clearance in the residual plots from the PRCC analysis. Therefore this could indicate that Q contributes to the variation in the system but without a clear relationship to the output. This argues for the need of an accurate estimate of Q to eliminate some of the noise in the system.

Table S2: *Host parameters showing significant PRCC with total Mtb, chromosomal equivalents or time to clearance at the end of treatment. Parameter categories refer to categories discussed in Table 1 in the main text.*

Parameter	**Parameter category**	Controls			INH			RIF		
		Tot Mtb.	Mtb CEQ[1]	Time To Clear	Tot Mtb.	Mtb CEQ[1]	Time To Clear	Tot Mtb.	Mtb CEQ[1]	Time To Clear
Number of host cell deaths causing caseation	Caseation	---	--	-			---	-		---
TNF threshold for causing apoptosis	TNF apoptosis		++		+	+++	++	+++	+++	+++
Rate of TNF induced apoptosis	TNF apoptosis	+++		+		---	++		---	+
Time steps before a resting macrophage can move	Cell movement						-			-
TNF threshold for activating NFkB	Mac activation	+++	+++	+++	+++	+++	+++	+++	+++	+++
Rate of TNF induced NFkB activation	Mac activation	---	---		---	---	---		---	---
Probability of resting macrophage killing bacteria	Resting macrophage killing					-	-		-	
Threshold for intracellular bacteria causing chronically infected macrophages	Time bacteria are intracellular					+++			+++	
Probability of an activated macrophage healing a caseated compartment in its Moore neighborhood	Caseation		+							
Probability of a T-cell moving to the same compartment as a macrophage	Cell movement	-	--		-	-	-		-	
IFNγ producing Tcell probability of inducing Fas/FasL mediated apoptosis	T cell-mediated killing					-				-
IFNγ producing Tcell probability of producing IFN	Mac activation	---	---		-	---	---		---	---
Cytotoxic T-cell probability of killing a macrophage	T cell-mediated killing									-
Macrophage maximal recruitment probability	Recruitment	++	++		+	+++	+++	+	+++	+++
IFNγ producing T-cell maximal recruitment probability	Recruitment	---	---			---	---	--	---	---
IFNγ producing T-cell half sat for chemokine recruitment	Recruitment						--			

-/+: $p < 0.01$; --/++: $p < 0.001$; ---/+++: $p<0.0001$

[1]: CEQ (chromosomal equivalents) or the number of bacterial genomes represents the cumulative bacterial load since it has been shown that bacterial genomes persist when bacteria are killed[9,23]. The difference between CEQ and CFU represents the degree of bacterial killing.

Table S3: *Antibiotic parameters and their correlation with antibiotic distribution (AUC and granuloma:lung ratio) and treatment outcomes (final total CFU and time to clearance). Parameters are listed followed by the sign of the PRCC (-/+: negative/positive correlation) and the rank of their correlation in brackets (Rank 1: most influential).*

	Plasma PK parameters	**Lung tissue PK parameters**	**PD parameters**
Total CFU	Plasma clearance rate (+) (1)	Degradation rate constant intracellular (+) (1) Effective diffusivity (-) (1) Cellular accumulation ratio (+) (1) Vascular permeability (-) (1)	Max activity intracellular (-) (1) Max activity extracellular (-) (1) C50 for intracellular Mtb (+) (1) Hill constant for intracellular Mtb (+) (1) Hill constant for extracellular Mtb (+) (1)
AUC in granuloma	Plasma clearance rate (-) (1)	Degradation rate constant intracellular (-) (1) Cellular accumulation ratio (-) (2) Vascular permeability (+) (1)	
Granuloma: Normal lung AUC ratio		Degradation rate constant intracellular (-) (1) Effective diffusivity (+) (2) Cellular accumulation ratio (-) (2) Vascular permeability (+) (1)	
Time to clearance	Plasma clearance rate (+) (2)	Degradation rate constant intracellular (+) (2) Cellular accumulation ratio (+) (2)	Max activity extracellular (-) (2) C50 extracellular non-replicating Mtb (+) (2) Hill constant for extracellular Mtb (+) (1)

2.2. Naïve Bayes classification.

This method uses early model outputs (day 100), called features, to make predictions about final model outputs (day 280). Using the features listed in Table S4, the Bayes classifier is able to predict treatment outcome with 82 - 90% accuracy for INH regimens and 80 - 87% accuracy for RIF regimens (Figure S4).

Table S4: *Pre-treatment features predictive of treatment outcomes using the Bayes classifier. Feature categories refer to categories discussed in Table 1 in the main text.*

Pre-treatment Feature	**Feature category**
Number of resting macrophages	Granuloma size
Number of infected macrophages	Intracellular CFU
Number of activated Tγ	T-cell activation
Number of IFN producing Tγ	T-cell-mediated killing
Number of Tcyt downregulated by Tregs	Tcell activation
Number of TNF producing Tcyt	Tcell activation
Intracellular CFU	Intracellular CFU
Non-replicating extracellular CFU	Non-repl CFU
Cumulative number of bacteria killed by TNF induced apoptosis	TNF apoptosis
Cumulative number of bacteria killed by cytotoxic Tcells	T cell-mediated killing
Cumulative number of bacteria killed by activated macrophages intracellularly	Mac activation
Cumulative number of bacteria that died in caseum	Caseation
Total TNF	Mac activation/ TNF apoptosis
Total IL10	Mac activation
Total chemokines	Recruitment and movement
Grauloma size	Granuloma size
Number of caseated compartments	Caseation
Number of caseated compartments healed	Caseation
Number of infected macrophage killed by TNF induced apoptosis	TNF apoptosis
Number of chronically infected macrophages killed by TNF induced apoptosis	TNF apoptosis
Number of infected macrophages with TNF induced NFkB	Mac activation
Number of Tcells killed by TNF induced apoptosis	TNF apoptosis
Number of macrophages killed by Fas/FasL induced apoptosis	T cell-mediated killing
Number of macrophages killed by cytotoxic Tcells	T cell-mediated killing
Number of macrophages exposed to Mtb	Mac activation
Cumulative number of activated Tgamma	Tcell activation
Cumulative number of activated Tcyt	Tcell activation
Cumulative number of activated Treg	Tcell activation
Average time spent intracellular per Mtb	Time spent intracellular per bacterium
Cumulative intracellular Mtb	Intracellular CFU

Cumulative extracellular non-replicating Mtb	Nonrep CFU
7 day AUC	AUC

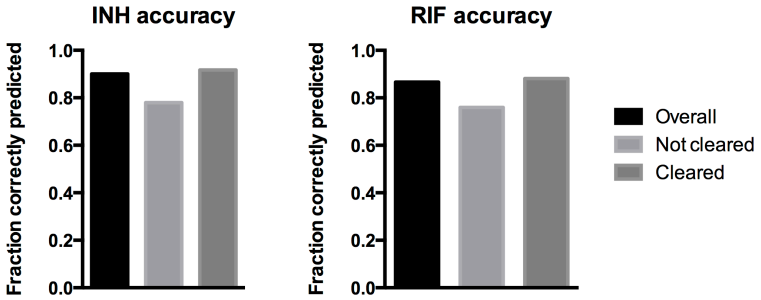

Figure S4: *Predictive accuracy of Bayes classification method based on selected subset of features described above. Accuracy is shown for cleared and non-cleared granulomas separately and the overall accuracy of the two groups combined.*

Each feature used for the Bayes classifier represents an output of the model at day 100 (pre-treatment), e.g. "Number of infected macrophage killed by TNF induced apoptosis" is a cumulative measure of how many infected macrophages have been killed by TNF-induced apoptosis in the first 100 days of infection. These features depend on the model parameters that we analyzed using PRCC, e.g. "TNF threshold for causing apoptosis". Together these two methods identify early predictors (features) of treatment success or failure as well as the mechanisms (parameters) that drive them.

3. Antibiotic pharmacokinetic and pharmacodynamics sub-model calibration

3.1. Plasma PK sub-model calibration

Parameter ranges sampled for fitting of NHP plasma PK indices are given in Table S5. These parameter ranges were guided by data values derived from rabbits [7] as well as from human studies[24,25].

Table S5: *Parameter ranges sampled for plasma PK calibration*

		Min	**Max**
INH	Absorption rate constant	1.00	5.00
	Intercompartmental clearance rate constant	0.02	0.20
	Plasma volume of distribution	0.10	2.00
	Peripheral volume of distribution	20.00	40.00
	Plasma clearance rate constant	0.20	2.00
RIF	Absorption rate constant	0.10	1.50
	Intercompartmental clearance rate constant	0.05	0.70
	Plasma volume of distribution	0.50	20.00
	Peripheral volume of distribution	0.10	2.00
	Plasma clearance rate constant	0.05	0.50

3.2. Tissue PK sub-model calibration

We calibrate the model using normal lung tissue and granuloma AUC observed in rabbits [7] by sampling parameter space for $k_{deg,i}$, $k_{deg,e}$, D, a, and p in the ranges given in Table S6. The ranges were guided by knowledge about pharmacochemical properties of INH and RIF[26-28]. Parameter values were selected that minimized differences between experimental measurements[7] and model predictions of AUC ratios relative to plasma. We discuss specific parameters in more detail below.

Table S6: *Tissue PK parameter ranges used for model calibration*

	RangeMin	**RangeMax**
INH		
Degradation rate constant extracellular ($k_{deg,e}$)	$1x10^{-10}$	$5x10^{-6}$
Degradation rate constant intracellular ($k_{deg,i}$)	$1x10^{-6}$	$1x10^{-2}$
Effective diffusivity (D)	$1x10^{-8}$	$1x10^{-6}$
Cellular accumulation ratio (a)	$3x10^{-1}$	1.3
Vascular permeability (p)	$1x10^{-7}$	$1x10^{-4}$
RIF		
Degradation rate constant extracellular ($k_{deg,e}$)	$1x10^{-10}$	$1x10^{-6}$
Degradation rate constant intracellular ($k_{deg,i}$)	$1x10^{-6}$	$1x10^{-2}$
Effective diffusivity (D)	$1x10^{-8}$	$1x10^{-6}$
Cellular accumulation ratio (a)	2	20
Vascular permeability (p)	$1x10^{-7}$	$1x10^{-4}$

Lung tissue PK calibration resulted in an estimated diffusivity (D) of $1.1x10^{-7}$ cm^2/s for INH. Experimental data for small molecule diffusion in granulomas is not available, but data from tumors (another densely packed cellular structure) can be used as an estimate. Our estimated diffusivity is on the same order as the diffusivity in tumors ($\sim 5x10^{-7}$ cm^2/s) obtained empirically taking size, lipophilicity and number of hydrogen donor and accepter sites into account[26]. It should be noted that based on molecule size alone, the estimated diffusivity for INH in tumors is $\sim 1x10^{-5}$ cm^2/s[27], suggesting that the physicochemical properties of INH limit its movement in tissue.

Lung tissue PK calibration resulted in an estimated vascular permeability (p) of $8.4x10^{-6}$ cm/s for INH. This is 1 log lower than the predicted vascular permeability in tumors based on size alone $1x10^{-4}$ cm/s[27]. However, given the effects of the physicochemical properties of INH on diffusivity it is possible that these properties also limit vascular permeability. We consider our estimate to be a lower limit of permeability since the rapid conversion of INH pro-drug to its metabolites can

result in an underestimation of experimentally measured concentrations in the rabbit granuloma data to which we are comparing[28].

Lung tissue PK calibration resulted in an estimated diffusivity (D) of $7x10^{-7}$ cm2/s for RIF. We anticipate low effective diffusivity of RIF since it is between 84 and 91% protein bound[29] and protein binding reduces effective diffusivity[30,31]. Indeed, the estimated diffusivity of small molecules in tumors obtained empirically taking size, lipophilicity and number of hydrogen donor and accepter sites (but not protein binding) into account is $\sim 1x10^{-6}$ cm^2/s[26]. Our predicted diffusivity for RIF is higher than the predicted diffusivity for INH despite the larger size of RIF, and is due to the high lipophilicity of RIF relative to INH. Model calibration resulted in an estimated vascular permeability (p) of $1x10^{-5}$ cm/s for RIF.

INH[32] and RIF[33] passively diffuse into host cells and differentially accumulate inside cells. Cellular accumulation ratios (ratio of intracellular to extracellular concentrations) have been measured in vitro in macrophages or in alveolar cells from patients[34-37]. Calibrated values for cellular accumulation ratios (a) of INH (0.35) and RIF (18) were within range of experimental observations: experimental cellular accumulation ratios vary between 0.45 and 1.03 for INH and between 2.5 and 16 for RIF[35-37].

3.3.PD sub-model calibration

In the case of INH, for the extracellular bacteria population, B_E, the $C_{50,BE}$ is set to the value for bacteria in broth culture 0.04 mg/L[38]. Intracellular bacterial population, growing in macrophage monolayers have been reported to have similar[39], lower[40,41] or higher[38] C_{50} than bacteria in broth culture[38]. We assume an equal apparent C_{50} which, due to lower host cell accumulation of INH[34], gives a $C_{50,BI}$ of 0.02 mg/L, half of $C_{50,BE}$. Since non-replicating bacterial populations are less susceptible to INH[42] but clearance of infection by INH is still observed in NHPs (Figure 2C)[8], $C_{50,BN}$ is set to 0.5 mg/L[42]. Intracellular maximum activity of INH is lower than extracellular maximum activity[38], and Emax values were calibrated to reproduce INH efficacy after 2 months of daily dosing as observed in NHP studies (Figure 2C)[8].

Similarly for RIF, the extracellular bacterial population, B_E, value for $C_{50,BE}$ is set to the value for bacteria in broth culture 1.2 mg/L[43]. Intracellular bacteria, B_I, in mouse macrophage monolayers had RIF $C_{50,BI}$ 2.5-fold higher than bacteria in broth culture, despite a more than 4-fold higher concentration inside cells than outside[35,36]. Since our model distinguishes between intracellular and extracellular concentrations of antibiotics we use a $C_{50,BI}$ of 10 mg/L for intracellular bacterial populations. Non-replicating bacterial populations (B_N) show reduced susceptibility relative to replicating population (4-fold increase in MIC) to RIF and so in this case $C_{50,BN}$ is set to 5 mg/L[42]. Intracellular activity of RIF is lower than extracellular activity[43], and Emax values were calibrated to reproduce RIF efficacy after 2 months of daily dosing as observed in NHP studies (Figure 2C)[8].

4. Supplemental Figures

4.1.Antibiotic concentration gradients as treatment progresses

In the main text we describe antibiotic exposure for the first day of treatment. In Figure S5 we show snapshots and antibiotic exposure for 160 and 260 d.p.i. for the same simulated granulomas discussed in the main text and shown in Figure 5. The differences in plasma PK parameters between the two granulomas are given in Table S7.

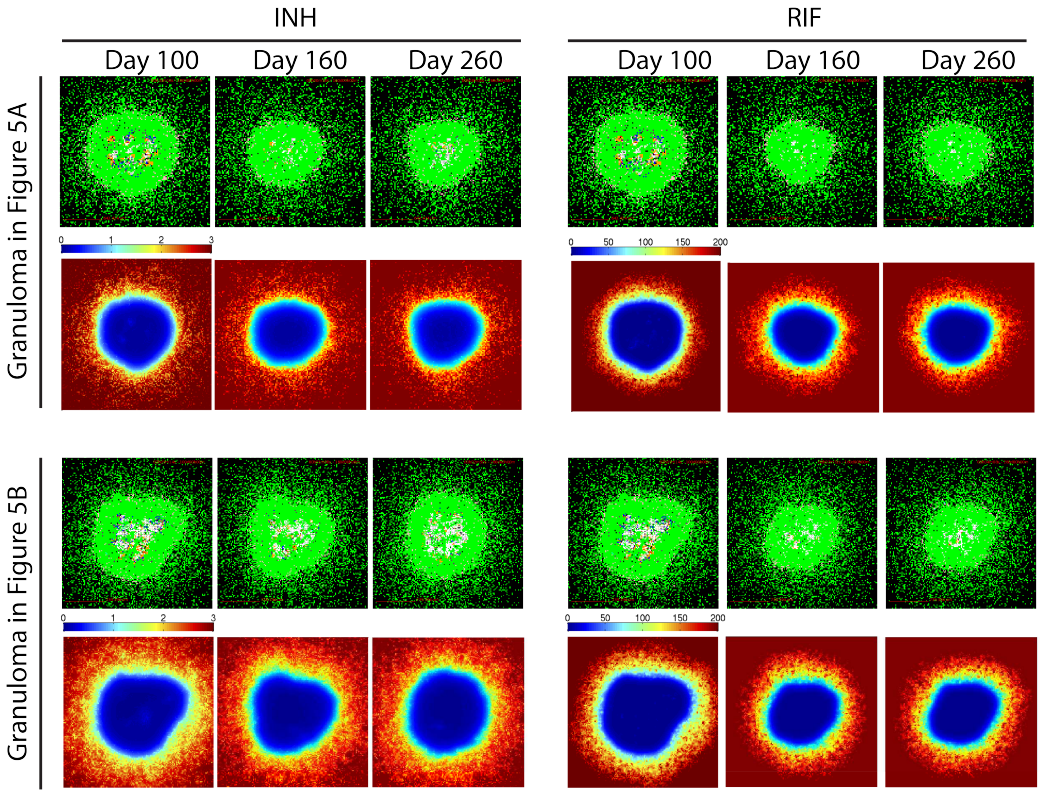

Figure S5*: Snapshots and 24 hour antibiotic exposure at three time points (100, 160 and 260 d.p.i) for the granuloma shown in Figure 5A (top) and the granuloma shown in Figure 5B (bottom). Antibiotic exposure is shown for INH (left) and RIF (right).*

Table S7: *Comparison of antibiotic parameters between granulomas shown in Figures 5A and 5B in the main text and Figure S5 above. Parameter units can be found in Appendix E in the main text.*

		Granuloma shown in Figures 5A and S4	**Granuloma shown in Figure 5B and S4**
INH	Absorption rate constant	4.81	4.18
	Intercompartmental clearance rate constant	0.07	0.13
	Plasma volume of distribution	0.68	1.97
	Peripheral volume of distribution	36.91	22.66
	Plasma clearance rate constant	1.12	1.67
RIF	Absorption rate constant	0.49	0.59
	Intercompartmental clearance rate constant	0.44	0.32
	Plasma volume of distribution	0.65	0.98
	Peripheral volume of distribution	0.71	0.83
	Plasma clearance rate constant	0.21	0.22

4.2. Proportions of bacteria killed by different mechanisms included in the model

In the main text we identify the importance of resting macrophage phagocytosis and killing of extracellular bacteria through phagosome-lysosome fusion (i.e. non-activated mechanisms) using sensitivity analyses. Figure S6 shows the proportion of bacteria killed by all mechanisms included in the model for untreated and treated granulomas. Only the bacterial killing that occurs between day 100 and 280 are included and for the treated granulomas the proportion of bacteria killed by antibiotics is excluded for this comparison.

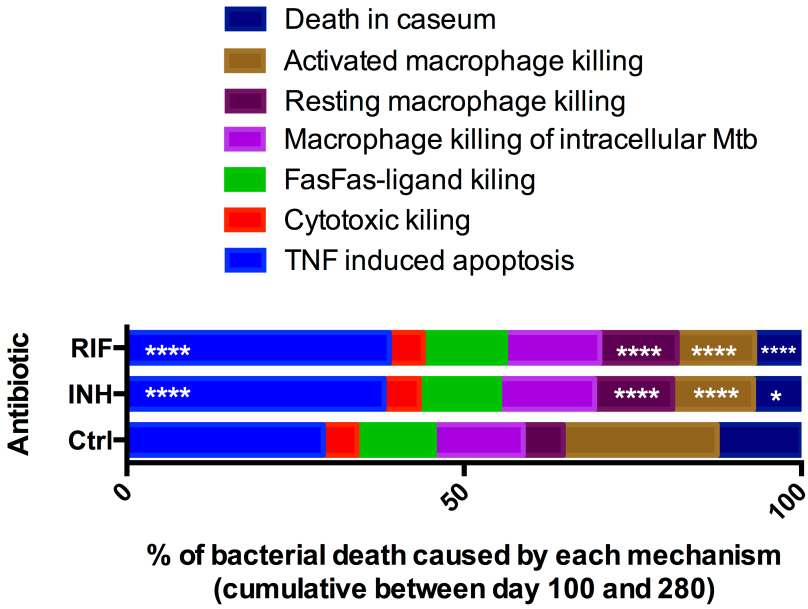

Figure S6: *Proportion of bacterial killed by host mechanisms differ between treated and untreated granulomas. For treated granulomas, bacteria killed by antibiotics are excluded for this comparison. Asterisks indicate significant differences between treated and untreated granulomas. *: p < 0.05, ****: p < 0.00005. Bars show mean proportions for 412 granulomas.*

References

1 Croley, A. N. *et al.* Lower capillarization, VEGF protein, and VEGF mRNA response to acute exercise in the vastus lateralis muscle of aged vs. young women. *Journal of applied physiology* **99**, 1872-1879, doi:10.1152/japplphysiol.00498.2005 (2005).

2 Ryan, N. A. *et al.* Lower skeletal muscle capillarization and VEGF expression in aged vs. young men. *Journal of applied physiology* **100**, 178-185, doi:10.1152/japplphysiol.00827.2005 (2006).

3 Gehr, P., Bachofen, M. & Weibel, E. R. The normal human lung: ultrastructure and morphometric estimation of diffusion capacity. *Respiration physiology* **32**, 121-140 (1978).

4 Gundersen, H. J. *et al.* Some new, simple and efficient stereological methods and their use in pathological research and diagnosis. *APMIS : acta pathologica, microbiologica, et immunologica Scandinavica* **96**, 379-394 (1988).

5 Kischell E, A. T. *Grid cycloid arc batch processor*, <http://rsb.info.nih.gov/ij/plugins/grid-cycloid-arc.html> (

6 Schneider, C. A., Rasband, W. S. & Eliceiri, K. W. NIH Image to ImageJ: 25 years of image analysis. *Nature methods* **9**, 671-675 (2012).

7 Kjellsson, M. C. *et al.* Pharmacokinetic evaluation of the penetration of antituberculosis agents in rabbit pulmonary lesions. *Antimicrobial agents and chemotherapy* **56**, 446-457, doi:10.1128/AAC.05208-11 (2012).

8 Lin, P. L. *et al.* Radiologic responses in cynomolgous macaques for assessing tuberculosis chemotherapy regimens. *Antimicrobial agents and chemotherapy*, doi:10.1128/AAC.00277-13 (2013).
9 Lin, P. L. *et al.* Sterilization of granulomas is common in active and latent tuberculosis despite within-host variability in bacterial killing. *Nature medicine* **20**, 75-79, doi:10.1038/nm.3412 (2014).
10 Cilfone, N. A., Perry, C. R., Kirschner, D. E. & Linderman, J. J. Multi-scale modeling predicts a balance of tumor necrosis factor-alpha and interleukin-10 controls the granuloma environment during Mycobacterium tuberculosis infection. *PLoS One* **8**, e68680, doi:10.1371/journal.pone.0068680 (2013).
11 Fallahi-Sichani, M., El-Kebir, M., Marino, S., Kirschner, D. E. & Linderman, J. J. Multiscale computational modeling reveals a critical role for TNF-alpha receptor 1 dynamics in tuberculosis granuloma formation. *J Immunol* **186**, 3472-3483, doi:10.4049/jimmunol.1003299 (2011).
12 Ray, J. C., Flynn, J. L. & Kirschner, D. E. Synergy between individual TNF-dependent functions determines granuloma performance for controlling Mycobacterium tuberculosis infection. *J Immunol* **182**, 3706-3717, doi:10.4049/jimmunol.0802297 (2009).
13 Kaneko, H. *et al.* Role of tumor necrosis factor-alpha in Mycobacterium-induced granuloma formation in tumor necrosis factor-alpha-deficient mice. *Laboratory investigation; a journal of technical methods and pathology* **79**, 379-386 (1999).
14 Flynn, J. L. *et al.* Tumor necrosis factor-alpha is required in the protective immune response against Mycobacterium tuberculosis in mice. *Immunity* **2**, 561-572, doi:1074-7613(95)90001-2 [pii] (1995).
15 Flynn, J. L. *et al.* An essential role for interferon gamma in resistance to Mycobacterium tuberculosis infection. *J Exp Med* **178**, 2249-2254 (1993).
16 Kirschner, D. E., Hunt, C. A., Marino, S., Fallahi-Sichani, M. & Linderman, J. J. Tuneable resolution as a systems biology approach for multi-scale, multi-compartment computational models. *Wiley interdisciplinary reviews. Systems biology and medicine* **6**, 289-309, doi:10.1002/wsbm.1270 (2014).
17 Costa, B. Spectral methods for partial differential equations. *CUBO* **6**, 1-32 (2004).
18 Fornberg, B. A Practical Guide to Pseudospectral Methods. *ZAMM - Journal of Applied Mathematics and Mechanics / Zeitschrift für Angewandte Mathematik und Mechanik* **77**, 798-798, doi:10.1002/zamm.19970771017 (1997).
19 Trefethen, L. N. *Finite Difference and Spectral Methods for Ordinary and Partial Differential Equations*. (Cornell University, [Department of Computer Science and Center for Applied Mathematics], 1996).
20 Mugler, D. H. & Scott, R. A. Fast fourier transform method for partial differential equations, case study: The 2-D diffusion equation. *Computers & Mathematics with Applications* **16**, 221-228, doi:http://dx.doi.org/10.1016/0898-1221(88)90182-4 (1988).
21 Deen, W. M. *Analysis of Transport Phenomena*. (Oxford University Press, 2012).

22 Gottlieb, D. & Shu, C.-W. *On the Gibbs Phenomenon and Its Resolution*. Vol. 39 (Society for Industrial and Applied Mathematics, 1997).
23 Munoz-Elias, E. J. *et al.* Replication dynamics of Mycobacterium tuberculosis in chronically infected mice. *Infection and immunity* **73**, 546-551, doi:10.1128/IAI.73.1.546-551.2005 (2005).
24 Wilkins, J. J. *et al.* Variability in the population pharmacokinetics of isoniazid in South African tuberculosis patients. *British journal of clinical pharmacology* **72**, 51-62, doi:10.1111/j.1365-2125.2011.03940.x (2011).
25 Wilkins, J. J. *et al.* Population pharmacokinetics of rifampin in pulmonary tuberculosis patients, including a semimechanistic model to describe variable absorption. *Antimicrobial agents and chemotherapy* **52**, 2138-2148, doi:10.1128/AAC.00461-07 (2008).
26 Pruijn, F. B., Patel, K., Hay, M. P., Wilson, W. R. & Hicks, K. O. Prediction of Tumour Tissue Diffusion Coefficients of Hypoxia-Activated Prodrugs from Physicochemical Parameters. *Australian Journal of Chemistry* **61**, 687-693 (2008).
27 Schmidt, M. M. & Wittrup, K. D. A modeling analysis of the effects of molecular size and binding affinity on tumor targeting. *Molecular cancer therapeutics* **8**, 2861-2871, doi:10.1158/1535-7163.MCT-09-0195 (2009).
28 Sarathy, J., Dartois, V., Dick, T. & Gengenbacher, M. Reduced drug uptake in phenotypically resistant nutrient-starved nonreplicating Mycobacterium tuberculosis. *Antimicrobial agents and chemotherapy* **57**, 1648-1653, doi:10.1128/AAC.02202-12 (2013).
29 Boman, G. & Ringberger, V. A. Binding of rifampicin by human plasma proteins. *European journal of clinical pharmacology* **7**, 369-373 (1974).
30 Thurber, G. M. & Weissleder, R. A systems approach for tumor pharmacokinetics. *PLoS One* **6**, e24696, doi:10.1371/journal.pone.0024696 (2011).
31 Chaplin, D. J., Olive, P. L. & Durand, R. E. Intermittent blood flow in a murine tumor: radiobiological effects. *Cancer research* **47**, 597-601 (1987).
32 Conte, J. E., Jr. *et al.* Effects of gender, AIDS, and acetylator status on intrapulmonary concentrations of isoniazid. *Antimicrobial agents and chemotherapy* **46**, 2358-2364 (2002).
33 Hoger, P. H., Vosbeck, K., Seger, R. & Hitzig, W. H. Uptake, intracellular activity, and influence of rifampin on normal function of polymorphonuclear leukocytes. *Antimicrobial agents and chemotherapy* **28**, 667-674 (1985).
34 Jeena, P. M., Bishai, W. R., Pasipanodya, J. G. & Gumbo, T. In silico children and the glass mouse model: clinical trial simulations to identify and individualize optimal isoniazid doses in children with tuberculosis. *Antimicrobial agents and chemotherapy* **55**, 539-545, doi:10.1128/AAC.00763-10 (2011).
35 Mor, N., Simon, B., Mezo, N. & Heifets, L. Comparison of activities of rifapentine and rifampin against Mycobacterium tuberculosis residing in human macrophages. *Antimicrobial agents and chemotherapy* **39**, 2073-2077 (1995).
36 Ziglam, H. M., Baldwin, D. R., Daniels, I., Andrew, J. M. & Finch, R. G. Rifampicin concentrations in bronchial mucosa, epithelial lining fluid, alveolar

macrophages and serum following a single 600 mg oral dose in patients undergoing fibre-optic bronchoscopy. *The Journal of antimicrobial chemotherapy* **50**, 1011-1015 (2002).

37 Forsgren, A. & Bellahsene, A. Antibiotic accumulation in human polymorphonuclear leucocytes and lymphocytes. *Scandinavian journal of infectious diseases. Supplementum* **44**, 16-23 (1985).

38 Jayaram, R. *et al.* Isoniazid pharmacokinetics-pharmacodynamics in an aerosol infection model of tuberculosis. *Antimicrobial agents and chemotherapy* **48**, 2951-2957, doi:10.1128/AAC.48.8.2951-2957.2004 (2004).

39 Dhillon, J. & Mitchison, D. A. Activity and penetration of antituberculosis drugs in mouse peritoneal macrophages infected with Mycobacterium microti OV254. *Antimicrobial agents and chemotherapy* **33**, 1255-1259 (1989).

40 Chanwong, S., Maneekarn, N., Makonkawkeyoon, L. & Makonkawkeyoon, S. Intracellular growth and drug susceptibility of Mycobacterium tuberculosis in macrophages. *Tuberculosis* **87**, 130-133, doi:10.1016/j.tube.2006.06.001 (2007).

41 Hartkoorn, R. C. *et al.* Differential drug susceptibility of intracellular and extracellular tuberculosis, and the impact of P-glycoprotein. *Tuberculosis* **87**, 248-255, doi:10.1016/j.tube.2006.12.001 (2007).

42 de Steenwinkel, J. E. *et al.* Time-kill kinetics of anti-tuberculosis drugs, and emergence of resistance, in relation to metabolic activity of Mycobacterium tuberculosis. *The Journal of antimicrobial chemotherapy* **65**, 2582-2589, doi:10.1093/jac/dkq374 (2010).

43 Jayaram, R. *et al.* Pharmacokinetics-pharmacodynamics of rifampin in an aerosol infection model of tuberculosis. *Antimicrobial agents and chemotherapy* **47**, 2118-2124 (2003).